CHAPTER 2
LIGHT SCATTERING AND RADIANCE IN THE ATMOSPHERE

With a view to develop approximate link-budget oriented atmospheric models, this chapter focuses on the elastic scattering processes (Rayleigh and Mie) that take place in the atmosphere at the visible and near-infrared wavelengths. The electromagnetic basis and comprehensive simulations of the scattering parameters are presented. Emphasis is given to Mie's situations such as clouds, hazes, fogs and rains, which are of prime concern in elastic lidar systems.

The flow of the text investigates simple analytic models that enable easy assimilation of the qualitative effects that temperature, pressure and humidity variables play on the scattering under standard atmospheric conditions. Examples focus on 1064- and 532-nm Nd:YAG wavelengths, though the relationships are also valid for other wavelengths.

The final part of the chapter is committed to solar and lunar irradiance assessment based on celestial coordinates. This can be a major interference to the lidar system.

All these points are integrated into a software package named *link-atmos*.

1. MODELS IN A STANDARD ATMOSPHERE APPROXIMATION

Temperature, pressure and air density at ground level as well as their height-profiles deserve special attention because of their influence on scattering. They will only be considered in the *troposphere* since most of the atmospheric scatterers (clouds, hazes, aerosols...) belong to this layer, that extends up to approximately 11 km. Its temperature usually decays with height [49][9],

$$\frac{\partial T}{\partial z} < 0 \qquad (1)$$

whereas its pressure can vary from 1 atm (1013 mb) to a few tens of milibars at the top boundary. Eq.(1) is equivalent to the neutral stability assumption, a standard atmosphere approximation that, in turn, implies a good mixture of the atmospheric constituents. Since the troposphere has a large energy and mass exchange with the surface, it is responsible for convection (winds). This relation also holds true for the *stratosphere* (up to *50-km* height), a highly stable layer characterized by long residence times. Between them, there is the *tropopause* (Fig.1), an unstable layer (positive temperature gradient).

The atmosphere is formed by gases and particles in suspension. Two basic types of gases can be distinguished depending on whether their concentration is permanent or variable. Permanent gases includes nitrogen, oxygen, argon and the like (see Tab.1 from [32] for their volume concentrations). They represent the 99.03% of the total volume and have constant volumetric proportions even though air density dwindles with height. The

variable gases, which basically encompas ozone (O_3), water-vapour (H_2O), carbon-dioxide (CO_2), carbon-monoxide (CO), nitric acid (HNO_3), ammonium (NH_3), hydrogen-sulphide (H_2S), sulphide-dioxide (SO_2), nitrogen-dioxide (NO_2) and nitrogen-oxide (NO), are of particular concern for their reactive and sometimes toxic effects. The concentrations of these gases are regulated and they must be determined locally as they can vary largely, both geographically and temporally. For them, volume proportions with height are not constant, which stands out as an important distinctive feature.

GAS		% VOLUME	ppm
Nitrogen	N_2	78.084	780840
Oxygen	O_2	20.946	20946
Argon	Ar	0.934	9340
Neon	Ne	$18.18 \cdot 10^{-4}$	18.18
Helium	He	$5.24 \cdot 10^{-4}$	5.24
Methane	CH_4	$1.6 \cdot 10^{-4}$	1.6
Krypton	Kr	$1.14 \cdot 10^{-4}$	1.14
Hydrogen	H_2	$0.5 \cdot 10^{-4}$	0.5
Nitrogen oxide	N_2O	$0.5 \cdot 10^{-4}$	0.5
Xenon	Xe	$0.087 \cdot 10^{-4}$	0.087

Tab.1 Permanent concentration gases.

PARTICLE TYPE	RADIUS (μm) from	to	CONCENTRATION (cm^{-3}) from	to
Water droplets	10^2	10^4	10^{-5}	10^{-2}
Clouds	1	10	10	300
Fogs	1	10	10	100
Aerosols	10^{-2}	1	10	10^3
Air molecules	10^{-4}		10^{19}	

Tab.2 Radii and concentrations for some particles.

As for the particles, not only do their chemical compositions vary, but also their radii (typ. from *0.01 μm* to *10 μm)*. Tab.2 from [32] lists some examples along with

typical concentrations. They comprise both aerosols and hydro-meteors. The former group of constituents or hazes have radii under *1 μm* and they are formed by smoke and dust in suspension. The latter embody water in liquid or solid state (rain, snow, etc.).

Gas absorption also plays an important part in computing the extinction-coefficient along the lidar beam path as it is directly related to the transmittance. Usually, polyatomic molecules increase their vibrational and rotational moments at the expense of the absorbed energy. In the visible and infrared band, water-vapour, carbon-dioxide, ozone and oxygen are the major absorbers. There are other gases, though in lower concentrations, such as carbon-monoxide, methane and nitrogen oxides *(NOX)* that absorb energy in these bands. Scientific programs such as LOWTRAN, MODTRAN, HITRAN, [43][86][32][91] assess the absorption based on the atomic parameters of the gas molecules. ***At the Nd:YAG wavelengths (1064 and 532 nm) gas absorption becomes negligible as these wavelenghts are located in a propagation window where no local line absorption structure or continuum absorption bands exist.*** This affirmation can be corrobrated by ref.[32], Fig.3 and Fig.4, which illustrate the spectrum at *1064-nm* wavelength.

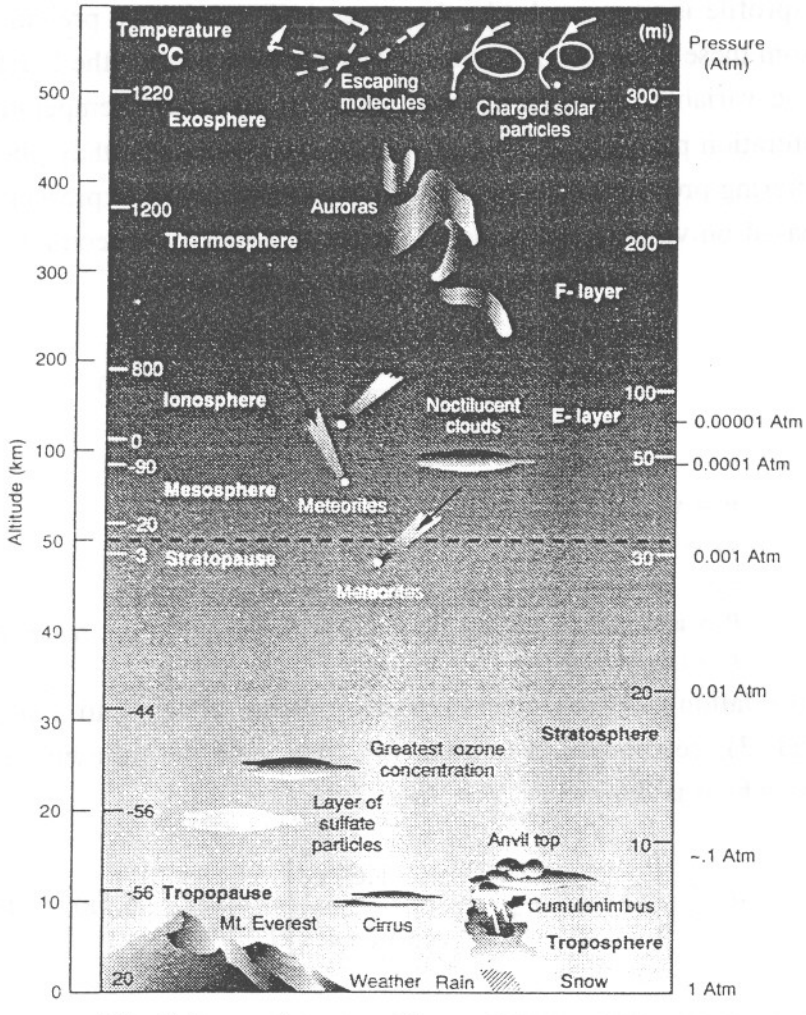

Fig.1 Atmosphere profile vs. height [105].

1.1 Standard atmosphere models

Back in 1991 the U.S. Air Force, U.S. Weather Bureau and NASA joined efforts to list the most important atmospheric parameters up to 100 km in what has been called the standard atmosphere model [37]. There, only permanent concentration gases are taken into account. Thus, a clear free-from-contaminant atmosphere is considered.

Within the troposphere, the following approximation is assumed for the *temperature* under stable conditions:

$$T(z) = T_o + az \tag{2}$$

As for the *pressure*, a similar relation is derived (Fig.5)

$$P(z) = P_o\left(\frac{T(z)}{T_o}\right)^{5.256} = P_o\left(1 - \frac{6.5z}{T_o}\right)^{5.256} \tag{3}$$

The last relation to be considered is the air density profile. Sensible default values can be a ground-level temperature of 288.15K and a surface air density of 1.255 Kg/m^3. Its height-profile is very much like that given in Fig.5 for the pressure.

From these relations, it is relatively easy to extrapolate the height-profiles of other atmospheric variables, such as the *refractivity*, the potential temperature and the water-vapour saturation pressure. They will be of special interest as they play a prominent role in the scattering processes. Based on [32][51], the following expression for the refractive index is based on vibrational-rotational studies of molecular spectra assuming Lorenztian profiles:

$$n = 1 + \left(237.2 + \frac{526.3\,\nu_1^2}{\nu_1^2 - \nu^2} + \frac{11.69\,\nu_2^2}{\nu_2^2 - \nu^2}\right)\frac{P}{T}10^{-6} \tag{4}$$

where:
- ν = wavenumber [cm^{-1}]
- ν_1 = 114.000 cm^{-1}
- ν_2 = 63.400 cm^{-1}
- P = atmospheric pressure [kPa] (1 atm = 1.013·10^5 Pa; 1 mb = 100 Pa)
- T = temperature [K]

This useful relation merges temperature and pressure effects into a single expression. If eqs. (2) and (3) are substituted into eq. (4), they yield the following expression for the *refractivity*, which is defined as $N = (n-1)\cdot 10^6$:

$$n = 1 + \left(237.2 + \frac{526.3\,\nu_1^2}{\nu_1^2 - \nu^2} + \frac{11.69\,\nu_2^2}{\nu_2^2 - \nu^2}\right)\frac{P_o}{T_o^{5.256}}(T_o - 6.5z)^{4.256}10^{-6} \tag{5}$$

Computations done within a typical 10 km margin have shown refractivity variations to be on the order of 200 ppm.

The *potential temperature* is often defined as the temperature one air volume would have if departing from an initial state of temperature T and pressure P, it reached *1000-mb* final pressure, under an adiabatic process of compression or expansion [88]. Formally,

$$\theta = T\left(\frac{1000mb}{P}\right)^{0.286} \tag{6}$$

This newly introduced term enables us to classify the atmosphere behaviour based on a *$\partial\theta/\partial z$-derivative sign* criterion. In case it is positive, the atmosphere becomes stable, neutral if zero, and unstable, otherwise [49].

Finally, *water-vapour saturation pressure* is defined as the water-vapour pressure that is needed to saturate the air (100 % relative humidity). It is given by [32]

$$E_s(T) = 24.096\left(\frac{300}{T}\right)^5 10^{\left(10-\frac{2950.2}{T}\right)} \tag{7}$$

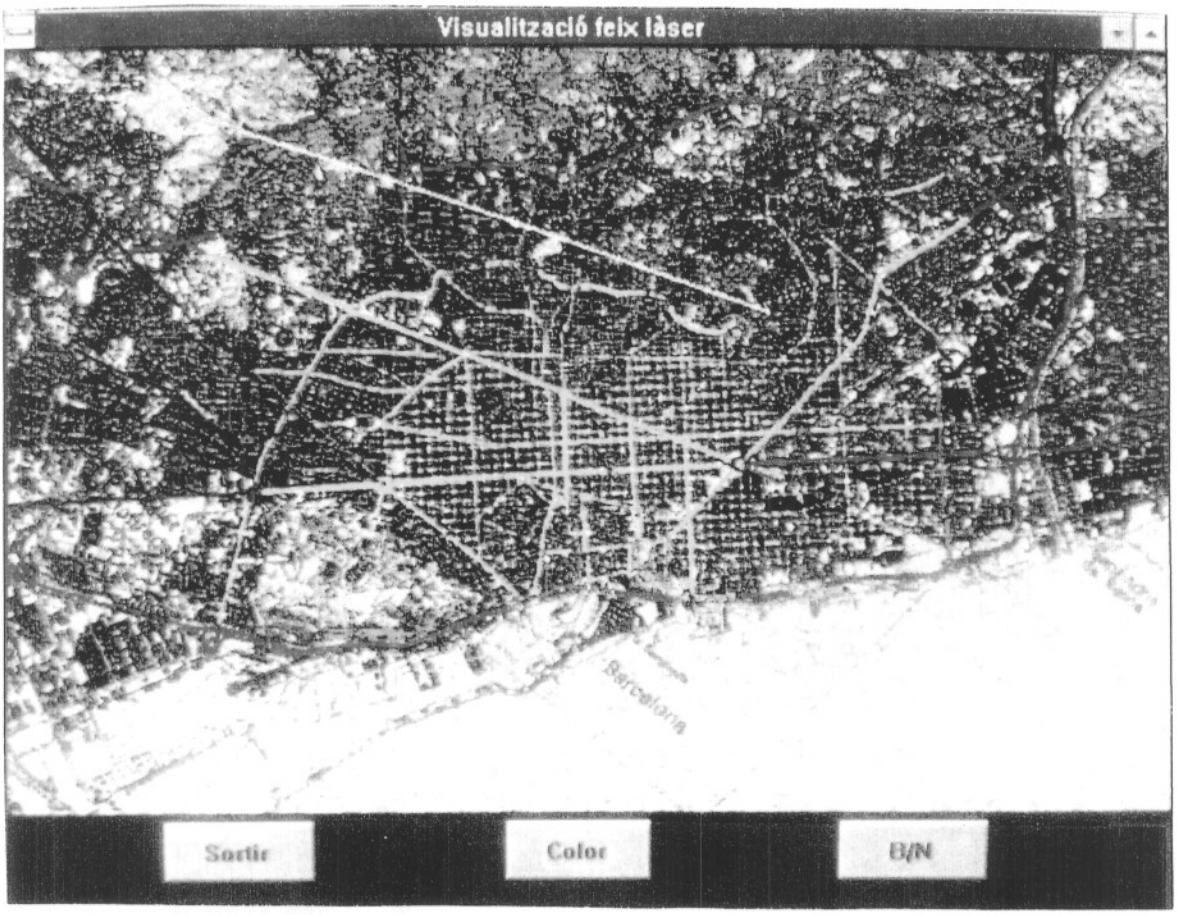

Fig.2 Simulation of the lidar beam-path (white) over the metropolitan area by **link-atmos.**

1.2 Data example for Barcelona

In order to bridge gulfs between the variables discussed in the previous sections and the different types of elastic scattering, Fig.6 to Fig.13 represent monthly histograms during 1992 (unless indicated otherwise) of the variables discussed in the previous section. They have been gathered by the Environment and Control Planning Unit of Barcelona's Council [38][40][41] from the network of meteorological stations. The same has been done for particle concentration (Fig.12) and pollutant gases like SO_2 (Fig.13). The raw data along with the models that will be presented in this chapter have been used in the final release of a software package named *link-atmos (Fig.2)*.

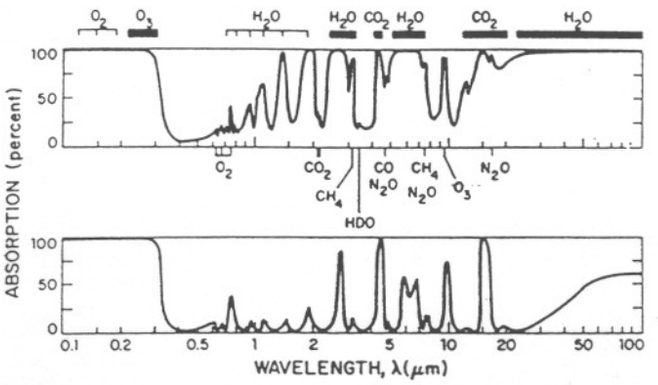

Fig.3 Coarse absorption spectrum due to atmospheric gases at ground level [9].

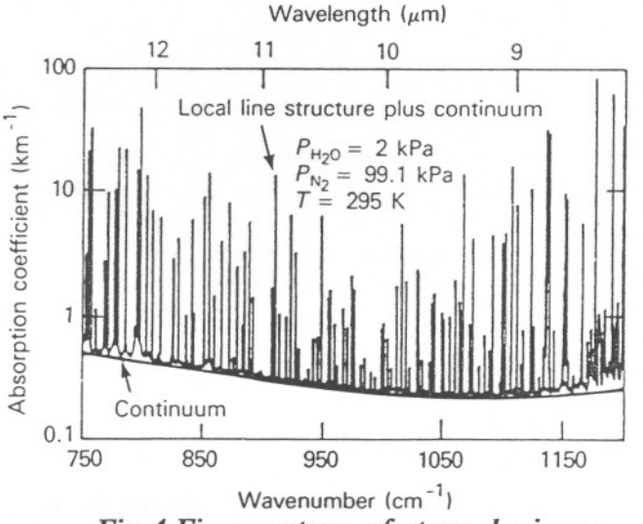

Fig.4 Fine spectrum of atmospheric gas absorption [105].

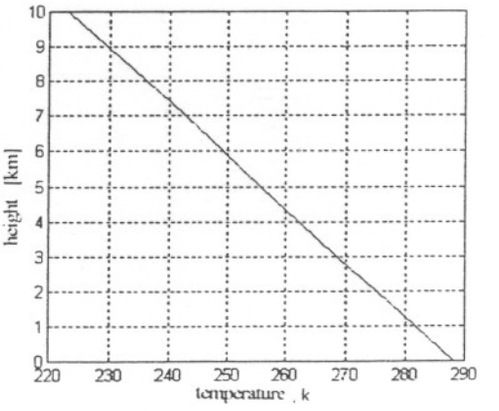

Fig.5 Atmospheric pressure profile vs. height.
$T_o = 288.15°K, P_o = 1013.25$ mb.

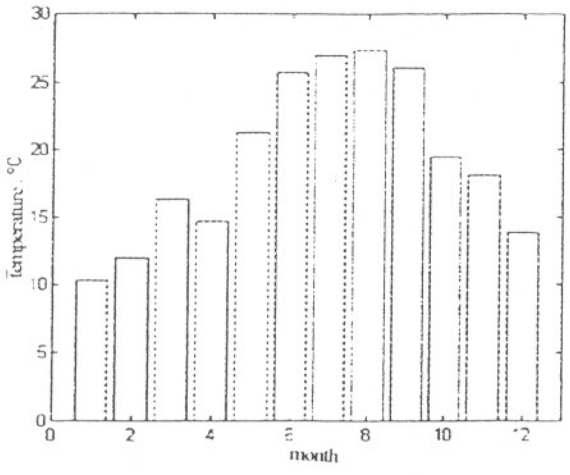

Fig.6 Monthly maximum temperatures.

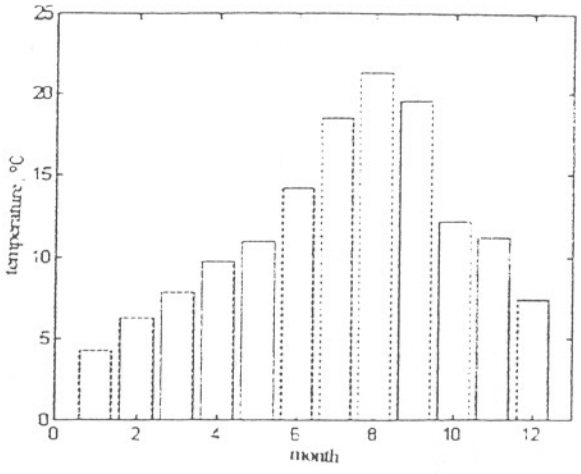

Fig.7 Monthly minimum temperature.

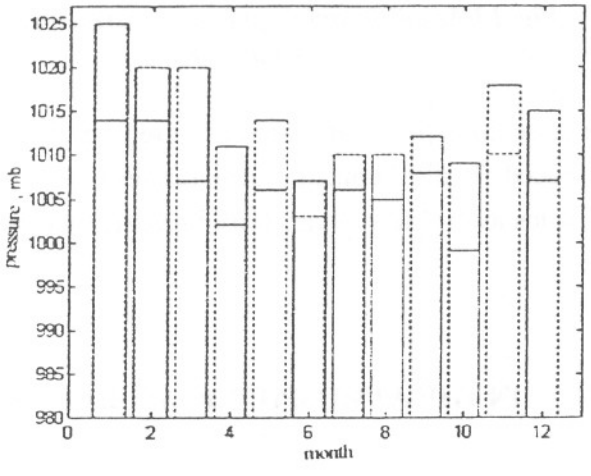

Fig.8 Monthly maximum and mean pressure.

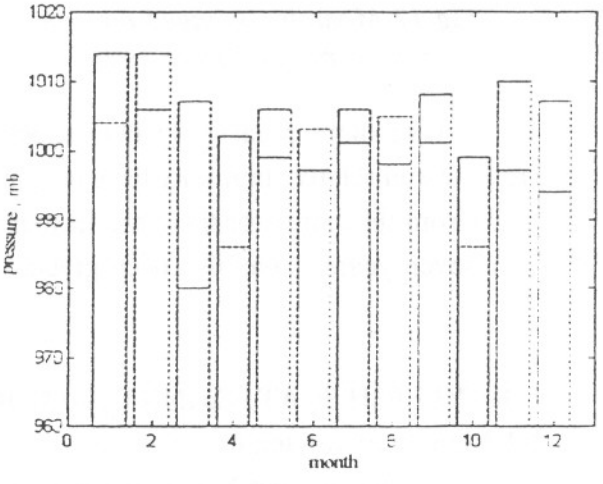

Fig.9 Monthly minimum and mean pressure.

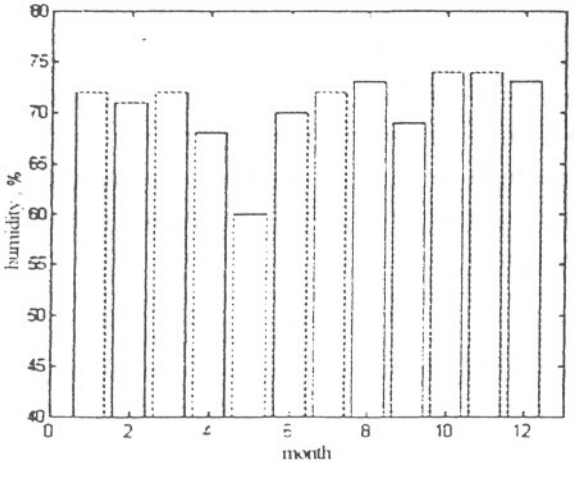

Fig.10 Monthly mean humidity.

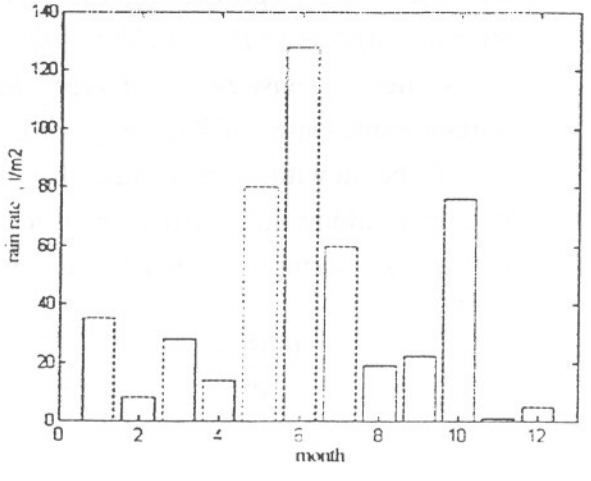

Fig.11 Monthly mean precipitation.

NOTE: Illustrations processed by ***link-atmos*** *based on 1992 raw-data provided by Diputació de Barcelona, U.O. de Planificació i Control de l'Ajuntament de Barcelona and Area Metropolitana de Barcelona (Entitat del Medi Ambient).*

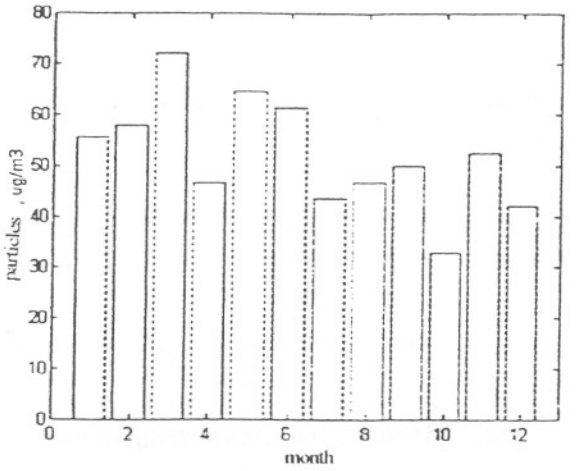

Fig.12 Monthly averaged particle concentration during 1993.

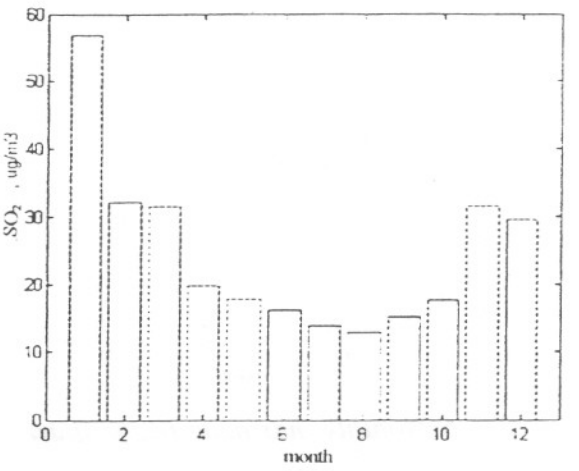

Fig.13 Monthly averaged concentration of SO_2 during 1993.

Up to here, measured values about the three main physical variables of temperature, pressure and relative humidity have been introduced. Typical concentration ranges over one year (from the simulator there are further statistics available such as daily or yearly values over seven years) have also been given.

2. RAYLEIGH SCATTERING DEPENDENCY ON THE ATMOSPHERIC VARIABLES

2.1 Review of Rayleigh scattering

It is far beyond our purposes to make an extensive review of this type of scattering as there are plenty of references on the subject [32][79][18][25] and it is a well known phenomenon. Before proceeding further it is worth remembering that *this type of scattering takes place whenever the particle radius is much lower than the wavelength,* otherwise Mie's scattering must be considered. Based on [32] and Fig.14, let us derive some important expressions of Rayleigh's cross-section.

To begin with, let us assume that incident light is polarized along the *x-axis* and that it propagates along the z^+-*axis*. Then, *Rayleigh's differential cross-section* per solid angle unit at any scattering direction θ,ϕ is given in spherical coordinates by

$$\frac{d\sigma(\theta,\phi)}{d\Omega} = \frac{\pi^2(n^2-1)^2}{N^2\lambda^4}(\cos^2\phi\cos^2\theta + \sin^2\phi) \qquad \left[\frac{m^2}{sr}\right] \tag{8}$$

where

n is the refraction index of the medium,

N is number density of the scatterers and,

λ is the wavelength of both the incident and scattered radiation.

If the incident light is unpolarized, the ϕ-*dependency* vanishes and the differential cross-section can be averaged out in ϕ at

$$\frac{d\sigma(\theta)}{d\Omega} = \frac{\pi^2(n^2-1)^2}{N^2\lambda^4}\left(\frac{1+\cos^2\theta}{2}\right) \tag{9}$$

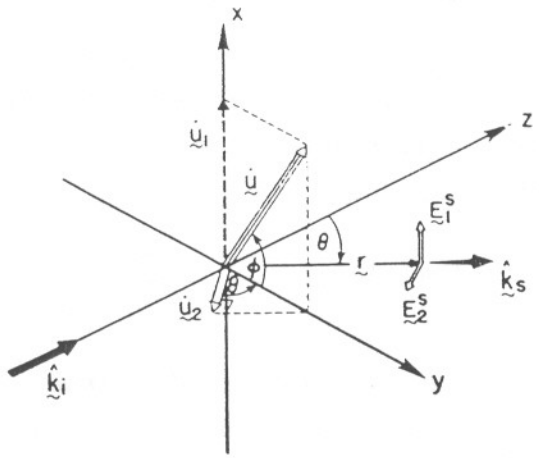

Fig.14 Angular components of the scattered electric field.

Regarding this result, it should be emphasized that the scattered light consists of two linearly polarized components, $I_\perp$ and $I_\parallel$, parallel and perpendicular, respectively, to the observation plane (see Fig.14). The $I_\perp$ is related to the unitary factor and, as a result, becomes independent of θ, while $I_\parallel$ is ruled by a $cos^2\theta$-factor.

Usually, this expression is corrected by the depolarization ratio p_n ($p_n = I_\perp/I_\parallel$) that accounts for anisotropic effects ($I \parallel (\theta=\pi/2) \neq 0$). Depolarization ratios for different gases can be found in [25]. If allowance is made for the anisotropic properties of the scattering molecules, eq.(9) takes the form

$$\frac{d\sigma(\theta)}{d\Omega} = \frac{\pi^2(n^2-1)^2}{N^2\lambda^4}\,\frac{1+\cos^2\theta}{2}\left(\frac{6+3p_n}{6-7p_n}\right) \tag{10}$$

The total cross-section $\sigma_R(\lambda)$ can be evaluated from eq.(8) by integrating over $\Omega = 4\pi$ *sr*

$$\sigma_R(\lambda) = \frac{8\pi}{3}\left[\frac{\pi^2(n^2-1)^2}{N^2\lambda^4}\right]\left(\frac{6+3p_n}{6-7p_n}\right) \tag{11}$$

Eqs.(10) and (11) can be related to each other by means of the *phase function* $P(\theta)$

$$\frac{d\sigma(\theta)}{d\Omega} = \frac{\sigma_R(\lambda)}{4\pi}P(\theta) \tag{12}$$

Formally, ***the phase function represents the angular dependency of the scattering and it is defined as the ratio of scattered energy per solid angle unit in a given direction to the scattered energy averaged out in all directions.***

Anisotropy is also an air characteristic. For this reason, a depolarization factor, $p_n = 0.035$ and the following expression for the phase function are often used

$$P(\theta) = 0.7629(1 + 0.9324\cos^2\theta) \tag{13}$$

The above results have paved the way to derive the expressions that model the optical coefficients, backscatter and extinction. ***The backscatter-coefficient, β_g, represents the scattering cross-section per unit-volume and solid angle unit at the observation angle $\theta=\pi$.*** It can be expressed mathematically as

$$\beta_g = N\sigma(\lambda,\theta=\pi) \approx \frac{\pi^2(n^2-1)^2}{N\lambda^4}\left(\frac{6+3p_n}{6-7p_n}\right) \tag{14}$$

where N is the density of molecules. Likewise, ***the blending of both absorption and scattering effects yields the extinction-coefficient, α_g.*** As it has been discussed, at the fundamental and second-harmonic wavelengths of the Nd:YAG laser only the latter should be considered. Thus, it can be written

$$\alpha_g = \alpha_{g,a} + \alpha_{g,s} \approx \alpha_{g,s} = N\sigma(\lambda) \tag{15}$$

2.2 Rayleigh scattering in a standard atmosphere

This section proceeds to estimate both Rayleigh's backscatter- and extinction-coefficients at the wavelengths of interest, based on ideal gases and homogeneous atmosphere assumptions. Though the resulting models are extremely simple, they serve the purpose to model approximately Rayleigh scattering phenomena in the atmosphere under varied conditions of temperature and pressure.

From the outset, the principle that the air-mass is formed by addition of the different gaseous masses in the mixture can be considered. This is equivalent to say that the air molar concentration is the sum of the molar concentrations of its components and can be formulated as follows

$$n_{air} = \sum_i n_i = n_{O_2} + n_{N_2} + n_{Ar} + \ldots \tag{16}$$

where n is expressed in *mols*. So as to compute the number of mols of a given gas, say n_i, one can resort to the ideal gases law [56][59], that can be written as

$$PV = nRT \tag{17}$$

where:

n: number of mols;

R: molar constant ($0.0825\frac{atm\cdot l}{mol\cdot K} = 8.314\frac{J}{mol\cdot K}$); (18)

and

T: gas temperature (K);
P: gas pressure (atm);
V: gas volume (l).

As long as height increases, atmospheric density decreases, so does the concentration of gases. However, as discussed when introducing the concept of permanent concentration gases, they maintain their proportions in volume. Therefore, one can resort to the Amagat's law, which states that a gaseous volume V at temperature T and pressure P formed by the mixture of two gases A, B, equals the sum of the partial volumes of the gases in the mixture V_A, V_B. Formally,

$$V = \sum_i V_i = V_A + V_B \tag{19}$$

In turn, as all the gases in the air undergo the same physical conditions of pressure and temperature, it can be formulated that

$$n_i = \frac{V_i P}{RT} \tag{20}$$

where V_i is the volume concentration of the *ith-gas* in the mixture.

If the oxygen is taken as an example, Tab.1 gives a volume concentration of 20.946 %, that is, 0.20946 m^3 out of 1 m^3 of air. The molar concentration per cubic meter can be computed using eq.(20) as

$$n_{O_2} = \frac{0.20946\ P}{RT} \tag{21}$$

Eventually, if the same eq.(20) is substituted back into eq.(16) air molar concentration can be estimated as a function of the temperature and pressure profile of eqs.(2) and (3). A new outcome is that *the concentration at a given height can be estimated whetherby knowledge of the physical variables, temperature and pressure, at that height or by using the standard atmosphere profiles, inputting the height itself.* Once the number of mols, n_{air}, is known, Rayleigh's backscatter and extinction can be estimated by substituting N_{air}, (*molecules/m^3*) which is related to the former parameter via the Avogadro's constant. (Note that in this notation, capital letters are used for molecular concentrations whereas lower-case ones for molar concentrations).

$$N_{air} = n_{air} N_{av} = n_{air} 6.023 \cdot 10^{23} \tag{22}$$

Another parameter that should be taken into account is the refractivity [35] on which Rayleigh scattering is directly dependent (eqs.(14) and (15)). It is clearly related to the temperature and pressure variables via eq.(4).

The following values have been produced by the program when inputting a temperature of 288.15K and a pressure of 1013.25 mb at ground level:

$$\begin{aligned} \alpha_{1.06} &= 8.218 \cdot 10^{-4} \quad km^{-1} \\ \alpha_{0.53} &= 1.361 \cdot 10^{-2} \quad km^{-1} \end{aligned} \tag{23}$$

$$\begin{aligned} \beta_{1.06} &= 9.639 \cdot 10^{-5} \quad km^{-1} sr^{-1} \\ \beta_{0.53} &= 1.597 \cdot 10^{-3} \quad km^{-1} sr^{-1} \end{aligned} \tag{24}$$

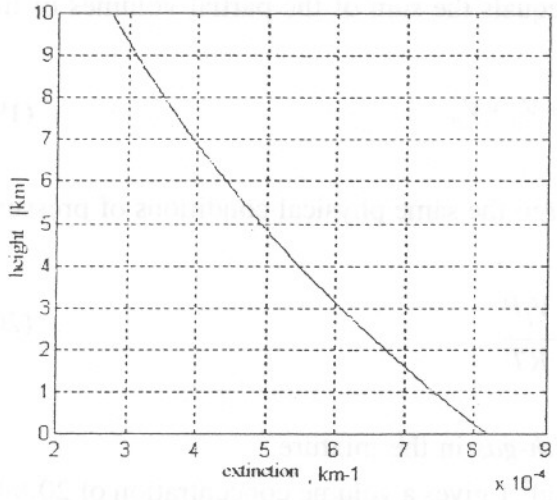

Fig.15 Rayleigh's extinction height profile.

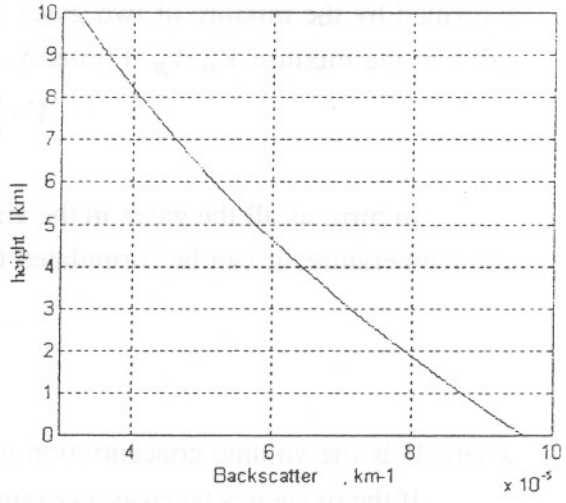

Fig.16 Rayleigh's backscatter height profile.

So as to corroborate them, we have resorted to the measurement campaign conducted by European Space Agency at Canary Islands (Spain) where this type of scattering was studied for the assessment of atmospheric losses on an optical link budget [51]. There, an empirical relation was derived that again took into account wavelength, pressure and temperature variables

$$\alpha_g = 2.9154 \cdot 10^{-4} \left(1 + 6.6 \cdot 10^{-3} \lambda^{-2}\right)^2 \lambda^{-4} \frac{P}{T} \tag{25}$$

If the same values of the example are substituted back into the equation above, it is found that they are in agreement with those introduced in eqs.(23) and (24). Notice that the reference did not consider refractivity variations, and that errors are under 1 %.

Another example of the possibilities of *link-atmos* is shown in Fig.15 and Fig.16 where Rayleigh's extinction in the air has been depicted vs. height in absence of pollutant sources (T=288.15K, P=1013.25 mb, λ=1064nm).

2.3 Inclusion of pollutant sources

For the time being, only permanent concentration gases have been considered when studying Rayleigh scattering effects. Yet, in the atmosphere, there are contaminant gases which do not maintain constant volume proportions. Obviously, their presence has to come about through an increment of the optical parameters figures obtained in the previous section. One might well wonder if these perturbations are noticeable.

Fist of all, let us reconsider eq.(17) in absence of contaminant sources

$$P_1 V_1 = n_1 R T_1 \tag{26}$$

Next, let us assume that a little concentration of contaminant is fed into the volume without disturbing its equilibrium. During the process the volume reamins constant at *1* m^3.

$$P_2 V_2 = n_2 R T_2 \tag{27}$$

The molar increment, Δn, yields a new P/T-relation, P_2/T_2. This implies that

$$\frac{P_2}{T_2} = \left(n_1 + \Delta n\right) R \tag{28}$$

Note that this formulation assumes $V_1 \approx V_2$, which is only true for small concentrations of the contaminating species. As in Sect.2.2, the extinction takes the form

$$\alpha_1 = A(\lambda)\frac{P_i}{T_i} \tag{29}$$

If eq.(28) is substituted into this last equation, the incremental extinction due to the contaminant source can be estimated by

$$\alpha_2 - \alpha_1 = A(\lambda) R \Delta n \tag{30}$$

To shed more light on the issue, let us consider the problem to assess the change in extinction due to the inclusion of a SO_2-limit concentration (under Barcelona's regulations) of *13* mg/m^3. Temperature and pressure figures are again *(T=288.15K, P=1013.25 mb)* and the problem is solved for the *1064-nm* wavelength.

As a result of computing it by *link-atmos*, it is assessed an incremental extinction of $3.94 \cdot 10^{-5}$ km^{-1}. Comparing this result back to eq.(23) it is one order or magnitude lower. This first guess may help to establish a detection threshold in Rayleigh LIDAR systems operated at these wavelengths. They usually work in the high troposphere and in the stratosphere. That is the case or *LIRA,* a Rayleigh LIDAR developed by SESO [113].

Quite different effects occur in the low troposphere. Chimneys for instance, have nothing to do with these figures, as their plumes contain particles whose radii belong to the Mie scale and which raise extinction figures several orders of magnitude. For this reason, the example applies at considerable heights (several kilometers) where Mie scattering is negligible.

3. MIE SCATTERING

3.1 Monodispersions

3.1.1 Review of Mie scattering

Mie scattering arises whenever the size of the scattering particle is comparable to or greater than the incident wavelength. The problem is usually formulated from the point of view of the electromagnetic theory and there are plenty of references [52][97][79][9][44][97][78], though approaches based on energy flux considerations are also found in the literature [32][12][17]. The way it is reviewed here is based on the first approach.

To begin with, let us model the scattering particle as a dielectric sphere of radius r and refractive index m, immersed in an homogeneous medium whose refractive index is normalized to unity. Incident light is x-polarized and propagates along the cartesian coordinate z^+. Working on this ground, the electric field vector can be expressed as

$$\begin{aligned} E(z,t) &= \hat{x}\, e^{j(\omega t - kz)} \\ H(z,t) &= \hat{y}\, e^{j(\omega t - kz)} \end{aligned} \tag{31}$$

If the wave equation is solved and adequate boundary constraints are imposed, the following solution is reached for the spherical components of the fields:

$$\begin{cases} E_\theta = H_\phi = -\dfrac{j}{kr}\cos\phi\, S_2(\theta) e^{j(\omega t - kr)} \\ -E_\phi = H_\theta = -\dfrac{j}{kr}\sin\phi\, S_1(\theta) e^{j(\omega t - kr)} \end{cases} \tag{32}$$

Regarding this result, it turns out that the scattered electric field is expressed in terms of two scalar components, S_1 and S_2, which are parallel and perpendicular, respectively, to the scattering plane (from which θ is measured). These components are called the Mie's scattering amplitude functions [97][32][52] and they can be written in series expansion form by

$$\begin{cases} S_1(\theta) = \displaystyle\sum_{n=1}^{\infty} \frac{2n+1}{n(n+1)} \left\{ a_n \pi_n(\cos\theta) + b_n \tau_n(\cos\theta) \right\} \\ S_2(\theta) = \displaystyle\sum_{n=1}^{\infty} \frac{2n+1}{n(n+1)} \left\{ b_n \pi_n(\cos\theta) + a_n \tau_n(\cos\theta) \right\} \end{cases} \tag{33}$$

In turn, π_n and τ_n can be developed in terms of Legendre's polynomials based on the angular dependency of the scattering. a_n and b_n account for Mie's complex coefficients.

Provided there is no depolarization of the incident radiation, Bohren and Huffman [44] gave a quite useful expression that related the parallel and perpendicular electric field components of the incident light with its scattering counterparts:

$$\begin{bmatrix} E_{\parallel}^{s} \\ E_{\perp}^{s} \end{bmatrix} = \frac{e^{jk(R-z)}}{-jkR} \begin{bmatrix} S_1 & 0 \\ 0 & S_2 \end{bmatrix} \begin{bmatrix} E_{\parallel}^{i} \\ E_{\perp}^{i} \end{bmatrix} \tag{34}$$

where R is the distance between the particle and the point under study.

Very often, these components are expressed in terms of the Stokes' vector and the Muller's matrix [15], which relates the Stokes' vectors of both incident and scattered light.

Letting alone further electromagnetic considerations, let us concentrate on the concepts of the intensity functions, efficiency factors, and the sought-after optical parameters, extinction and backscatter.

Intensity functions have very much to deal with the amount of scattered energy that splits between the parallel and perpendicular components, as it has been seen in eq.(33). These components are proportional to the intensity functions, $i_1(\theta)$ and $i_2(\theta)$, and they can easily be expressed in terms of the scattering components as

$$\begin{aligned} i_1(\theta) &= |S_1(\theta)|^2 \\ i_2(\theta) &= |S_2(\theta)|^2 \end{aligned} \tag{35}$$

Efficiency factors are dimensionless parameters that relate the scattering cross-section of a particle of radius r, σ_{sca}, to its geometrical one. The scattering efficiency, Q_{sca}, is defined as

$$Q_{sca} = \frac{\sigma_{sca}}{\pi r^2} \tag{36}$$

Likewise, the extinction efficiency merges into a single expression both absorption and scattering effects

$$Q_{ext} = \frac{\sigma_{ext}}{\pi r^2} = \frac{\sigma_{abs} + \sigma_{sca}}{\pi r^2} = Q_{abs} + Q_{sca} \tag{37}$$

The subscripts *ext, abs* and *sca* stand for extinction, absorption and scattering, respectively.

Were the particle not to be absorbing (i.e. the refractive index were a real number), all the incident energy would be scattered and both concepts, extinction and scattering, would coincide. These important efficiencies can be computed by series expansion from the a_n-, and b_n-coefficients as follows

$$\begin{aligned} Q_{sca} &= \frac{2}{x^2} \sum_{n=1}^{\infty} (2n+1) \left\{ |a_n|^2 + |b_n|^2 \right\} \\ Q_{ext} &= \frac{2}{x^2} \sum_{n=1}^{\infty} (2n+1) Re(a_n + b_n) = \frac{4}{x^2} Re(S_i(0)) \end{aligned} \tag{38}$$

As it has previously been introduced, the *x-term* or size parameter, is a straightforward way to relate the particle radius, r, to the wavelength, λ. It is defined as

$$x = kr = \frac{2\pi}{\lambda} r \tag{39}$$

Likewise, if an observation angle of *180°* is considered, the backscatter efficiency takes the form

$$Q_{back} = \frac{4}{x^2} |S_1(\pi)|^2 \tag{40}$$

From these relations, it arises that whenever $Q > 1$, the particle interaction with the incident radiation exhibits a cross-section higher than the geometrical one. Therefore, the particle perturbates the electric-field further than their own limits.

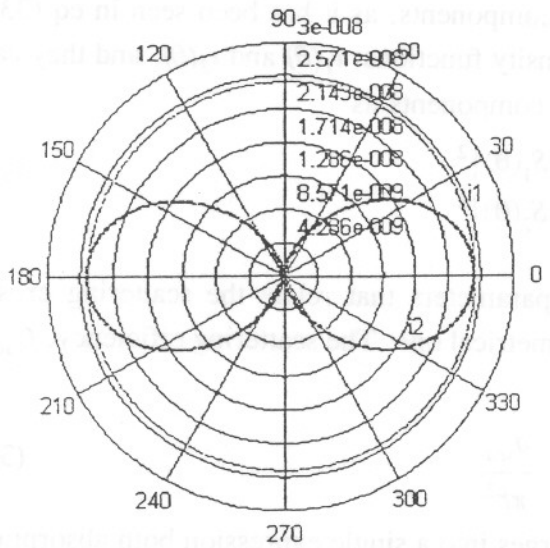

Fig.17 Intensity functions for x=0.1.

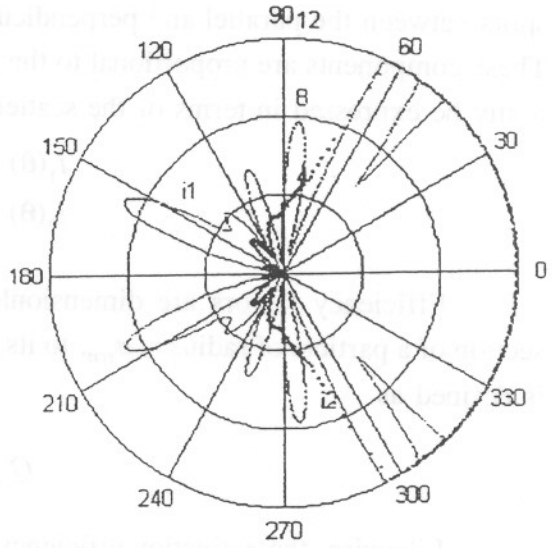

Fig.18 Intensity functions for x=8.

Finally, the scattering volume-coefficients, α and β, account for the extinction and backscatter cross-sections per unit volume under the assumption that the particles are spherical, anisotropic and independent of the incident light polarization. If one assumes that the interactions which take place are completely independent from each other (single-scattering assumption), the scattered flux becomes additive and one can be write

$$\alpha_{p,s} = N\sigma_{sca} = N\pi r^2 Q_{sca} \tag{41}$$

where N is the particle concentration per cubic meter.
Likewise, the net extinction can be estimated by using

$$\alpha_p = N\sigma_{ext} = N\pi r^2 Q_{ext} \tag{42}$$

By difference of eqs. (41) and (42), the absorption term can easily be obtained as

$$\alpha_{p,a} = \alpha_p - \alpha_{p,s} \tag{43}$$

The backscatter-coefficient can also be related to the particle density and to the backscatter efficiency as

$$\beta_p = N\pi r^2 Q_{back} \tag{44}$$

3.1.2 Simulation of monodispersions with link-atmos

Link-atmos software tackles Mie's monodispersions by considering parameters such as efficiencies vs. size parameter, refractive indexes, intensity functions, phase functions, angular dependencies, etc. Before the program was validated, many trial runs were conducted until the results released were successfully correlated with appropriate references [52][97][79].

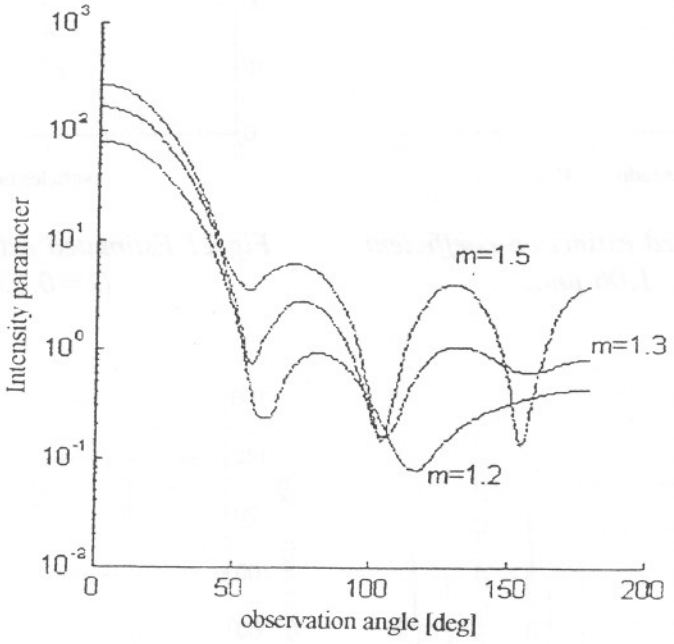

Fig.19 i_1-intensity function for $x=4$.

Fig.17 and Fig.18 show polar diagrams representing the perpendicular and parallel components of the intensity functions i_1, i_2, the refractive index being $m=1.25+j0$ and the size parameter values, $x=0.1$ and $x=8$. Quite different behaviours arise. On the one hand, when small values of the size parameter (much less that unity) are chosen, the plots resemble Rayleigh scattering ones, as they should. Consider, for instance, the radiation diagram symmetry, the $cos^2\theta$-dependency of the parallel component or the θ-independence of the perpendicular one (eq.(9)).

On the other hand, if size parameters larger than 0.5 are fed into the algorithms, the asymmetry becomes more and more relevant, which is in good agreement with Mie's theory, from which the ratio of forward-scattered energy to the backscattered one increases when so does the particle radius.

As far as it regards to the observation angle, θ, Fig.19 represents the perpendicular intensity component, $i_1(\theta)$, for different values of the refractive index. Complex indexes are also allowed in the program.

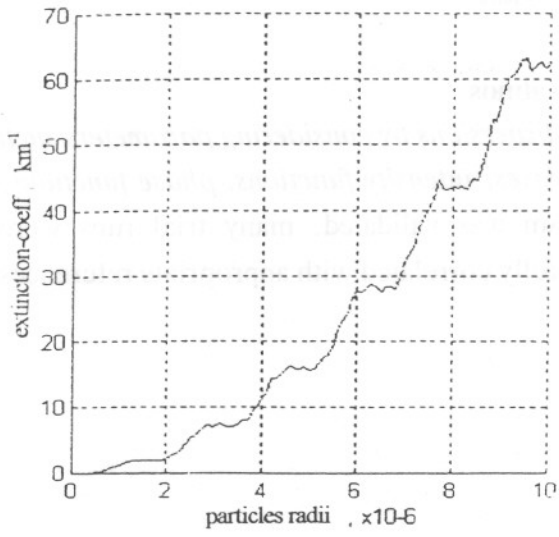

Fig.20 Estimated extinction-coefficient ($\lambda=1.06$ μm).

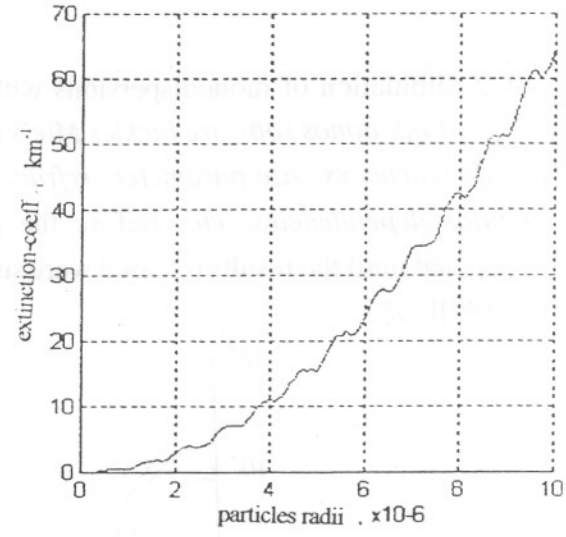

Fig.21 Estimated extinction-coefficient ($\lambda=0.53$ μm).

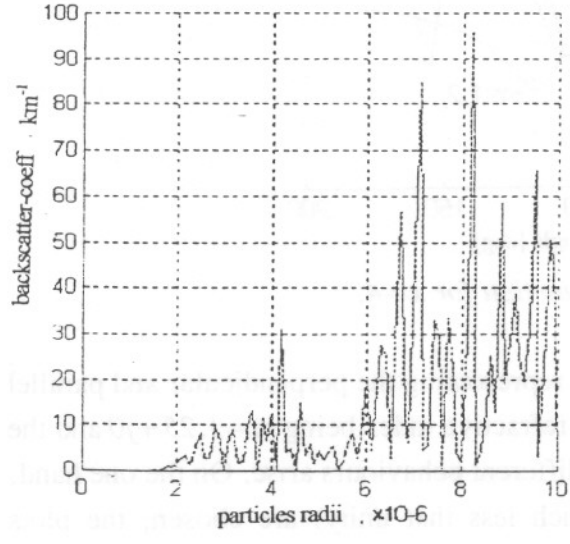

Fig.22 Estimated backscatter-coefficient ($\lambda=1.06$ μm).

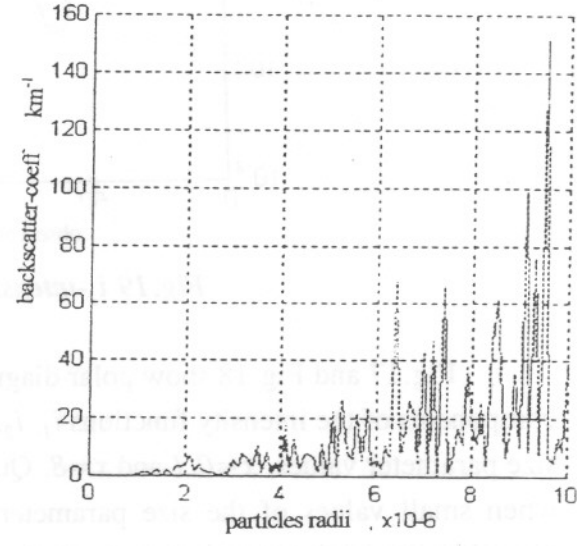

Fig.23 Estimated backscatter-coefficient at $\lambda=0.53$ μm-wavelength.

Fig.20 and Fig.21 consider a similar study at the Nd:YAG wavelengths (1064 and 532 nm) where the optical parameters have been estimated versus different particle radii for a concentration of 100 part/cm^3. The radii were chosen to be in good agreement with typical sizes of hydro-meteors, for which the water content is dominant. Regarding this fact, a real refractive index of $m=1.33$ was assumed as its imaginary part is negligible at these wavelengths [65]. Hale and Querry [46] suggested that the assumption could also be

extrapolated to dry particles provided relative humidity were near to or above 80 %. At these levels, water-vapour tends to condensate onto their surface.

By inspection of these figures the behaviour of the computed extinctions is very much the same. In both cases, there is a quadratic increase of the optical parameters with the radius (see Sect.3.1.1) together with superimposed oscillations due to the oscillating behaviour of the cross-section efficiency. These basic features are still re-encountered in Fig.22 and Fig.23 though the oscillations there are much larger.

3.2 Polydispersions

Seldom are scatterers monomodally distributed. On the contrary, their radii distribute along a density-size function. After a brief introduction on the subject, some of the most commonly used distributions together with their plots will be presented based on information gathered from various references (among them [79][52][97][25][9]). In the end, a rough link-budged oriented model for the city of Barcelona will be discussed. At this point, the main aim will be to take into account height and humidity effects on the optical parameters. Under no circumstance is meteorological forecast or physical weather modelling intended.

3.2.1 Optical parameters in polydispersions

Let $n(r)$ be a distribution function that for each radius, r, represents the concentration of particles (part/cm^3) whose radii are between r and $r+dr$. Then, the particle volume concentration, N, can be obtained as

$$N = \int_0^\infty n(r)\,dr \tag{45}$$

The extinction- and backscatter-coefficient in the case of polydispersions can easily be computed by using the extended form of eqs. (42) and (44) where the concentration term, N, has been substituted for the function $n(r)$. One can write:

$$\alpha_p = \int_0^\infty \pi r^2 Q_{ext}(r,\lambda)\,n(r)\,dr \tag{46}$$

Likewise, a similar expression can be written for the backscatter-coefficient or any other of the monodispersive parameters introduced in Sect.3.1. *Link-atmos* simulator will follow an analogous procedure. In addition, the user is allowed to choose from a large variety of density functions, which have been tabulated from different sources in the literature. Once chosen, intensity functions, phase functions, Muller coefficients and optical parameters are computed.

Before proceeding further, the available distributions from the simulator menu are considered:

3.2.2 Distribution functions

Reasonable approximation of real distributions is achieved by using power, log-normal and exponential-like laws in the models.

Amongst those of the first type, Junge's function [90] consists in a power-law of the form

$$n(r) = cr^{-(\beta+1)} \tag{47}$$

where:

c is a normalization constant accounting for the total concentration of particles,

β is a shaping parameter.

Shaping parameter values $2 \leq \beta \leq 4$ are often suitable for aerosols whose radii range between *0.1 μm-10 μm*, and for particles whose concentration rapidly decays beyond *0.1-μm radius* [35]. Values $3 < \beta < 4$ are frequent among hazes, while $\beta = 2$ is often used to model many types of fog [93].

In the second place, *log-normal distributions play an excellent role when modelling polydispersions*. They take the form [68][74]

$$n(r) = \frac{N}{(2\pi)^{\frac{1}{2}}\sigma_g r} \exp\left[-\frac{(\ln r - \ln r_m)^2}{2\sigma_g^2}\right] \tag{48}$$

where:

r_m is the modal radius (μm),

σ_g is the standard deviation or shaping parameter of the distribution and,

N is the total concentration of particles.

There exist other types of logarithmic functions that may be found in the literature such as the zero-order logarithmic function (ZOLD) [68], though they are not so frequent.

On top of power or log-normal laws and perhaps one the most often used distributions, there is the Deirmendjian function. It is a blend of the first two types. Formally, it is written as

$$n(r) = ar^{\alpha}\exp(-br^{\gamma}) \qquad 0 < r < \infty \tag{49}$$

Frequently, it is addressed as the modified gamma function, for both coincide when $\gamma = 1$.

The three parameters, a, b and γ are real-positive numbers, while α is an integer number. These are not independent from each other as their values depend on the kind of particles being modelled.

DISTRIBUTION TYPE	α	a	b	N (cm^{-3})	W ($g \cdot m^{-3}$)	R_N (μm)	R_M (μm)	ext (km^{-1})
Heavy fog, advective	3	0.027	0.3	20	0.37	10.	20.	28.74
Moderate fog, radiative	6	607.5	3.	20	0.02	2.	3.	8.672
Cumulus	3	2.604	0.5	250	1.	6.	12.	130.8
Stratus	2	27.0	0.6	250	0.29	3.33	8.33	55.18
Stratus/ strato-cumulus	2	52.734	0.75	250	0.15	2.67	6.67	35.65
Alto-stratus	5	6.268	1.111	400	0.41	4.5	7.2	91.04
Nimbo-stratus	2	7.676	0.425	200	0.65	4.7	11.76	87.08
Cirrus	6	$2.21 \cdot 10^{-12}$	0.09375	0.025	0.06405	64.	96.	1.011
Thin cirrus	6	0.011865	1.5	0.5	$3.128 \cdot 10^{-4}$	4.	6.	0.0831

NOTES:
1) R_N and R_M are the modal radii for number density and mass, respectively.
2) Extinction (ext) is specified at *0.55 μm*.
3) The parameter γ is unity for all models.

Tab.3 Deirmendjian's distribution parameters [105].

Integration of eq.(49) for all radii yields the expression that relates the total concentration of particles to the size parameters:

$$N = a \int_0^\infty r^\alpha \exp(-br^\gamma)\, dr = a\gamma^{-1} b^{-\left(\frac{\alpha+1}{\gamma}\right)} \Gamma\left(\frac{\alpha+1}{\gamma}\right) \tag{50}$$

From inspection of the equation, it emerges that the variable a is directly linked to the concentration. The remaining parameters, b, α, γ determine the *modal radius, r_c. This is to say, the radius for which a peak concentration occurs.* Mathematically,

$$r_c = \left(\frac{\alpha}{\gamma b}\right)^{\frac{1}{\gamma}} \tag{51}$$

Usually, the *b-parameter* is set from knowledge of the modal radius, whereas α and γ are fitted from experimentation. Yet, whenever computer assessment of the optical parameters, extinction and backscatter, is desired, the simulator will choose them from a look-up table containing the tabulated sets of each kind of distribution. Some Deirmendjian's ones are reproduced in Tab.3 [90][92]. Besides, the user can also choose from power- or logarithmic-law models.

As an example, Fig.26 plots H,L,M-type haze distributions. The latter, which stands for marine haze, comprises coastal and marine particles [67][53]. Haze L models continental aerosols and haze H is used for aerosols of stratospheric origin and tiny particles (dust). By inspection of Fig.26, it arises that haze H exhibits larger concentrations of small-size particles and sharper decaying slopes than the other two types, as it is the case.

Simulation of Deirmendjian's M- and L-type-rain distributions are shown in Fig.24. The M-type is the haze M counterpart for water drops and it is a sensible approximation in instances of intense rain, contrary to the L-type, which is used for light rains.

As far as clouds are concerned, Fig.25 plots alto-stratus, strato-cumulus, cumulus, stratus and nimbo-stratus distributions. Cloud shape features and constituents can be found in references [5][54][58]. The up-to-date classification available from the simulator [93] comprises nearly all kind of clouds (in addition to those mentioned, there are included cirrus and thin cirrus), advective heavy fog, radiative moderate fog and hails [87][64].

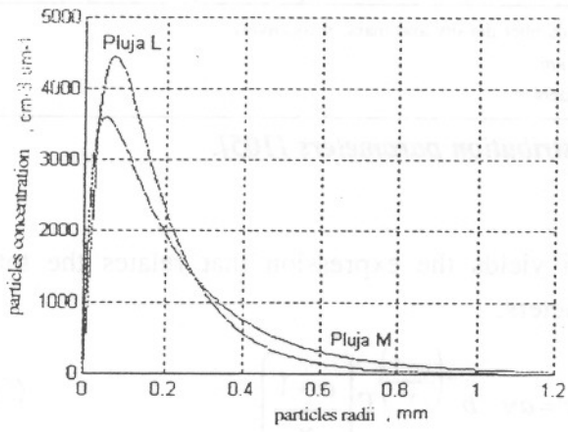

Fig.24 Distribution functions of L,M-type rains.

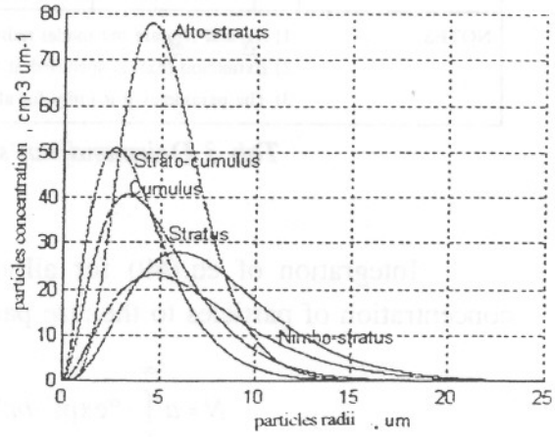

Fig.25 Distribution functions of different types of clouds.

4. HINTS TO BUILD LIDAR LINK-BUDGET-ORIENTED ATMOSPHERIC MODELS

4.1 Barcelona city example

In this section, a straightforward example of how a rough link-budget-oriented atmospheric model can be built is presented [71]. It is based on the case of the mediterranean urban industrial city of Barcelona. Yet, it has to be cautioned that its scope is clearly limited to link-budget assessment studies in typical day-to-day situations of optical transmittivity and visibility margin.

Besides, regarding that simple analytic models are more suitable for lidar inversion algorithms, as they usually work on the basis of data fitting onto some kind of adaptive model, this idea has been at the helm of the bibliographic research. Thus, even though the

values given are based on corroborated references, they should be understood as initial guesses to those inversion algorithms that would tackle the retrieval of physical atmospheric parameters (e.g. humidity) from extinction and backscatter data [187][186].

The aerosol distributions propounded by Deirmendjian are, in first approximation, appropriate for the kind of particles that can be found in a local area. Predictably, aerosol composition of the atmosphere cannot be thought to solely consist in one distribution of particles, on the contrary, it should be defined as a weighted sum of different distributions. Tab.4 lists typical aerosol volume mixtures along with their size distributions for continental, urban industrial and maritime models. Refractive-index figures are also indicated at the wavelengths of interest.

MODEL	SIZE DISTRIB	COMPONENT	% VOL	COMPLEX INDEX $\lambda=0.53\mu m$	COMPLEX INDEX $\lambda=1.06\mu m$
Continental	Fine	Water soluble	29		
	Coarse	Dusk-like	70		
	Fine soot	Soot	1		
Urban-industrial	*Fine*	*Water soluble*	*61*	$1.53\text{-}j5\cdot10^{-3}$	$1.52\text{-}j1.7\cdot10^{-2}$
	Coarse	*Dust-like*	*17*	$1.53\text{-}j8\cdot10^{-3}$	$1.52\text{-}j8\cdot10^{-3}$
	Fine soot	Soot	22		
Maritime	*Oceanic*	*Oceanic*	95	$1.381\text{-}j4\cdot10^{-9}$	$1.36\text{-}j6.01\cdot10^{-5}$
	Fine	Water soluble	5		

Tab.4 Aerosol mixture models.

From Tab.4 a sensible choice for the city would correspond to a *urban industrial model*. Yet, considering [105] the marine influence on the city can be accounted for by substituting the *fine soot* component by a *oceanic* one whose volume proportions were the same (22 %). Thus, the outcoming mixture can be worked out as the superposition of three log-normal distributions

$$n(r)=\sum_{n=1}^{3}\frac{N_i}{\ln 10\,(2\pi)^{\frac{1}{2}}\sigma_i r}\exp\left[-\frac{(\log r-\log r_i)^2}{2\sigma_i^2}\right] \qquad (52)$$

If the individual concentration of each species, N_i, is written in the form of $N_i = w_i Nt$, w_i stands for its individual weight in the urban industrial model (Tab.4) and N_t for the total concentration. Fig.26 compares Barcelona's model with Deirmedjian's H-,L- and M-type hazes. All plots assume $N_t = 100\ part/cm^3$. In the figure, a large population of particles with low radii and only one modal radius around 30-40 nm (rather than three) is noticeable. This is because the water-soluble component outweighs the two others in the mixture.

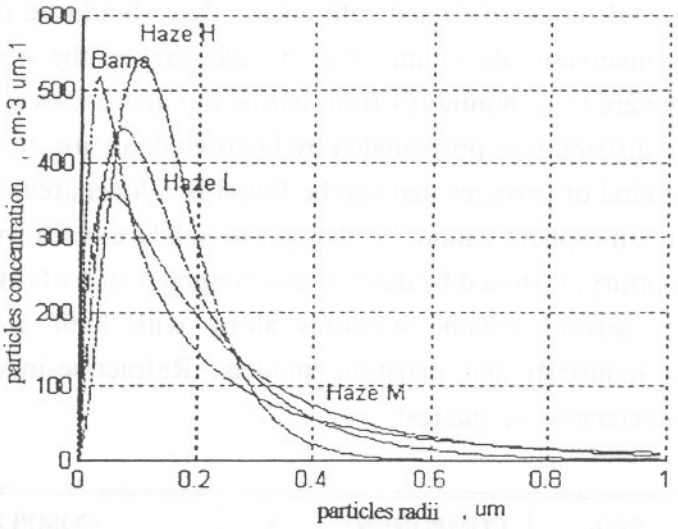

Fig.26 Comparison of Barcelona's model with Deirmedjian's hazes H,L and M.

4.2 Inclusion of humidity effects

Water-vapour plays a most important role in scattering theory since it is responsible for strong changes in the size-distribution of particles. It seems sensible to guess that the higher the humidity, over certain condensation level, the larger the particle radii will be, as the smaller ones will cluster round. As a result, the increase in the population of large-radius particles will occur at the expense of a shrinkage of the low-radius ones [74][180][204]. These are some of the models found in the literature:

Fitzgerald [60] addresses the point for marine particles based on the following model:

$$D(S) = D_d G(S) \qquad [\mu m] \tag{53}$$

$$G(S) = 0.81 \exp\left(\frac{0.066 S}{1.058 - S}\right) \qquad [\,] \tag{54}$$

where:

D is the actual particle diameter,

D_d is the particle diameter at a 80 % relative humidity and,

S is the saturation ratio relative to a relative humidity of 80% *(i.e. S = rh(%)/80)*

The above equations are substituted into the density function in the following way

$$n(D) = n'[D_d G(S)]\, G(S) \tag{55}$$

where $n'(D)$ represents the distribution at a 80-% relative humidity level.

The Wells, Gal and Munn model [100] applies to both particles of marine and continental origin. The dependency with humidity can be formulated as

$$r = Fr_o \tag{56}$$

$$F = 1 - 0.9\ln(1 - RH) \tag{57}$$

where:

r is the actual radius,

r_o represents the particle radius at *80-%* relative humidity level and,

RH is the relative humidity.

Contrary to these models based on an empirical approach, there are others, like the Shettle and Fenn one, that lay on a physical basis, taking into consideration parameters such as the chemical activity of water, dry and condensed mass, etc. [94]. On top of them, the Gathman model [62] is very often used for particles whose radius is log-normally distributed. It assumes that continental particles' radius does not depend on humidity while marine ones do so via a growing factor, f_c,

$$f_c = \left[\frac{c_7 - RH}{c_8(1 - RH)}\right]^{\frac{1}{2}} \tag{58}$$

where c_7, c_8 are modal constants for each kind of particles [62][63].

Resuming the Barcelona example, this is how the humidity has been modelled in the size-distributions of the computer code of link-atmos:

$$n(r) = \sum_{n=1}^{3} \frac{N_i}{\ln 10\,(2\pi)^{\frac{1}{2}}\,\sigma_i r} \exp\left[-\frac{(\log r - \log(f_{c,i} r_i))^2}{2\sigma_i^2}\right] \tag{59}$$

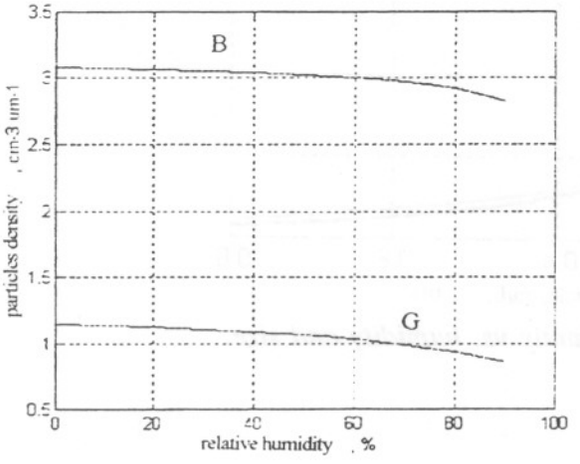

Fig.27 0.1μm-particle density change vs. humidity.

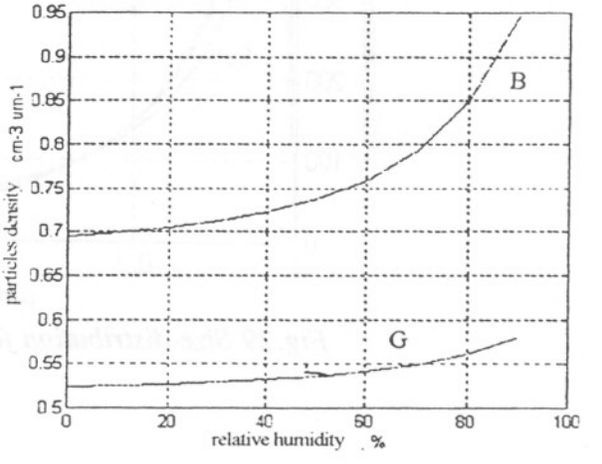

Fig.28 0.4μm-particle density change vs. humidity.

*NOTE: Letters **B** and **G** in Figs.(27) and (28) stand for eq.(59) and Gathman model [62], respectively.*

Although, constants c_7 *and* c_8 for *fine* and *coarse* particles should be measured in-situ, their figures have been extrapolated from a comparative study with the *Navy Aerosol Model (NAM) [62][61]*. The constants have been fitted by adjusting the humidity behaviour of the model to that of the NAM campaign over different mediterranean countries. Fig.27 and Fig.28 compare NAM measured values of *0.1-μm* and *0.4-μm particles* to those given by eq.(59). In both figures, the overall behaviour is retrieved. Note that differences in the absolute values are irrelevant since they can be offset by changing the total concentration of particles *(100 cm^{-3})*.

Fig.29 depicts a size-distribution family for different humidity levels. Once the family is assessed, extinction and backscatter vs. the relative humidity can be computed by the simulator. This has been done for the *1064-nm* wavelength and the resulting plot is shown in Fig.30. Quite similar plots (within 10% variations) are obtained at 532 nm. Note that the humidity criterion suggested by Wells and Shettle is also retrieved in the figure by a gradual change in slope beyond the *80-%* relative humidity value. The results of Fig.30 can be justified if one considers that the clustering of small particles onto the surface of bigger ones implies a net increase in the radius of the particle, which according to the trend shown in Fig.20 and Fig.21 gives higher extinction and backscatter values.

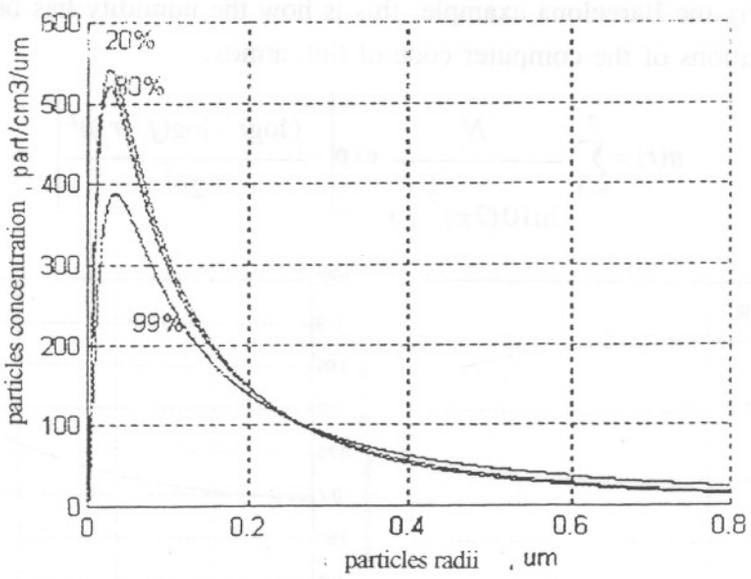

Fig.29 Size-distribution family vs. humidity and size.

4.3 Height dependency

Different aerosols spread over different atmospheric layers [32]. Each one is ruled by a physical mechanism that determines the type, density and size-distribution of them [69][70]. The first and lowest one spans from ground level to the boundary layer [49], which is located at about 2 km height; between 2 and 6 km there is a region where the concentration of particles undergoes an exponential decay with height; further up, between

6 and 30 km, there is the stratospheric layer. Finally, above 30 km, there are other layers whose main constituents are particles of extra-atmospheric origin. Above all, *the boundary layer deserves special attention for between it and ground level, meteorological conditions like water-vapour variations, exert a major influence on aerosol and particle distributions.* ***Despite this fact, it is often assumed that the concentration of particles below the boundary layer is a constant, N(0), which is independent from height*** as it is imposible to forecast their behaviour using the engineering-like approximations at hand. The relations presented next concentrate on ranges under *6-km height* that, as it will be shown in due course, are likely to be under the sensible operation ranges of the LIDAR.

For the layer extending between 2 and 6 km, the following formula

$$N(z) = N(0)\exp\left(-\frac{z}{z_s}\right) \tag{60}$$

underlines the exponential decay, where *N(0)* stands for the concentration at 2 km. Equivalently, this concentration coincides with that at ground level, because of the approximations discussed above. z_t is a scaling factor whose typical values range between *1-1.4 km*. A typical value for *N(0)* is $N(0) = 100\ cm^{-3}$ [65].

Fig.31, obtained with *link-atmos simulator*, assesses extinction- and backscatter-parameters vs. height for a haze M at 1064 nm based on eq.(60). The constant and exponential intervals in the two layers discussed are clearly seen in the figure.

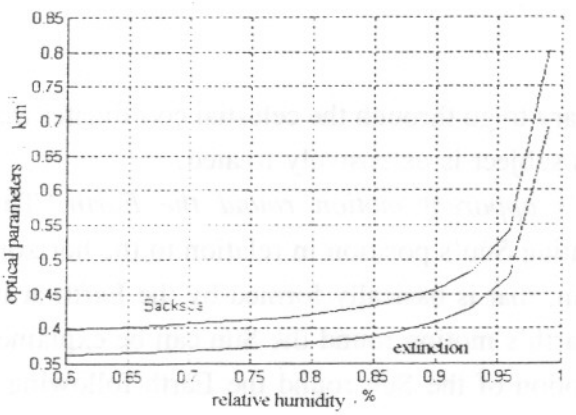

Fig.30 Extinction and backscatter vs. humidity (λ=1.06μm).

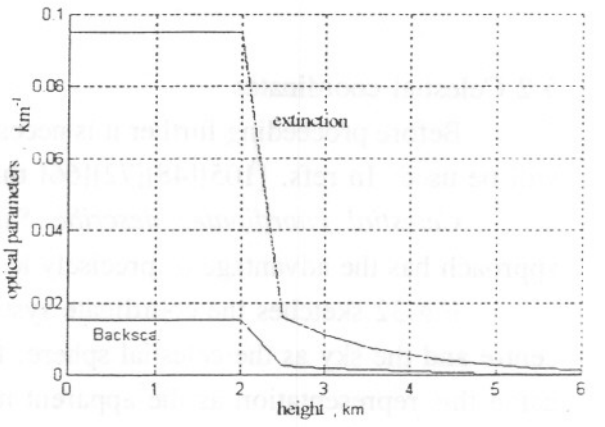

Fig.31 Extinction and backscatter vs. height (Haze M, λ=1.06μm).

5. THE BACKGROUND RADIANCE

5.1 Noisy sources

Every body that emits or reflects radiation at the wavelength of interest is considered a noise source since it is liable to interfere with the lidar-return-signal at the receiver front-end.

There are many sources of noise, but the most important are listed next:

- *The Sun:* By far, it is the most important for its strength and blackbody spectrum (see Sect. 5.3 and Fig.33).
- *The Moon:* It is the second most important source as it plays a prominent role at night.
- *The Sky:* The sky radiation is basically due to Rayleigh and Mie scattering of Sun's radiation by the atmospheric constituents. It is often called diffused radiation (see Sect. 5.3).
- *Ground-radiation:* This arises as a result of ground-reflection of the incoming radiation from external sources. It is know as the albedo component (Sect. 5.3).
- *Celestial bodies:* Mainly made by stars and other celestial bodies, figures greatly depend on the type of stars and their concentration. In spite of this fact, it is the least important of all and will not be treated here [105][98][73][39].

In the future, the concepts of irradiance $[W m^{-2}]$ or flux density, radiance or optical power emitted per unit area and solid-angle $[W m^{-2} sr^{-1}]$ and its spectral counterpart, the spectral irradiance $[W m^{-2} \mu m^{-1} sr^{-1}]$ will be taken for granted when assessing background radiance levels ([26] gives some insight into these concepts).

5.2 Celestial coordinates

Before proceeding further it is necessary to go through the celestial coordinates that will be used. In refs. [105][48][72][66] this subject is extensively treated.

Celestial coordinates describe Sun's apparent motion round the Earth. This approach has the advantage of precisely locating Sun's position in relation to the horizon.

Fig.32 sketches the coordinate system, that is basically formed by the Earth at its centre and the sky as the celestial sphere. Earth's motion round the Sun can be explained using this representation as the apparent motion of the Sun round the Earth following a circle that is tilted 23.45° on the terrestrial equator. The Sun travels this circle, once a year and the celestial sphere spins once a day round the earth, which remains fixed. Therefore, the Sun describes a circle whose diameter changes every day. It is maximum during the equinoxes and it is minimum during the solstices.

As far as it concerns to the celestial coordinates, some definitions should be made:

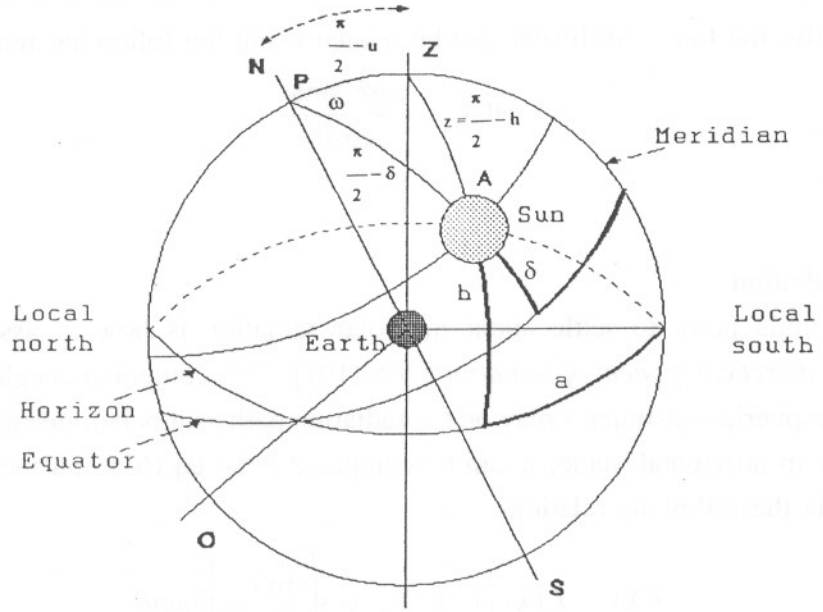

Fig.32 Celestial coordinate system.

The local vertical of a place intersects the celestial sphere at two points called zenith, Z and nadir, Z'. The complementary angle between this line, ZZ', and the polar axis, NS, is named the latitude, u. The maximum circle which is perpendicular to the observer is called celestial horizon. The celestial coordinates are formed by the azimuth, a, and the elevation over the horizon, h. The former is measured with respect to the local South, which results from the intersection of the local meridian (NZS) and the horizon (positive coordinates are towards the West). The latter represents the angular distance between the Sun and the horizon, counted on the vertical plane that includes the zenith (Z).

As for the temporal equatorial coordinates, the hourly angle is defined as the angular distance measured on the equator between the local meridian and the Sun's one, while the declination δ, as discussed, is the Sun-equator's angle measured on the Sun's meridian.

Considering the cosine-law in the spherical triangle APZ, one can write:

$$\sin h = \sin u \cdot \sin\delta + \cos u \cdot \cos\delta \cdot \cos\omega \tag{61}$$

where, the declination, δ, and the hourly angle, ω, are expressed by

$$\begin{cases} \delta = 23.45\dfrac{\pi}{180}\cdot\sin\left[(284+d_n)\dfrac{360}{365}\right] \\ \omega = \dfrac{360}{24}t \end{cases} \tag{62}$$

In these expressions, $d_n \epsilon (1,365)$ represents the current day and t, the time in hours.

Finally, the four coordinates can be related using the following relationship:

$$\sin a = \frac{\cos\delta \cdot \sin\omega}{\cos h} \tag{63}$$

5.3 Solar radiation

The main point to settle about the solar radiation is how to assess the *extra-atmospheric direct component of radiation* [105][101]. This component neglects the effects that the atmospheric constituents play on the radiation path as it penetrates the atmosphere.

Over an horizontal plane, it can be computed from eq.(61) and the solar spectral irradiance via the following relation:

$$I(\lambda) = I_o(\lambda) \cdot \left[1 + 0.033 \cdot \cos\left(\frac{360}{365} d_n\right)\right] \cdot \sin h \tag{64}$$

If, on the other hand, the telescope is aimed at a point whose local coordinates are *(h,a)* while the Sun is located at *(h',a')*, the *sin(h)* term in eq.(61) must be replaced by the dot product of their unit vector position

$$\hat{r}_{OA} \cdot \hat{r}_{OA'} = \cos h \cos h' \cos(a - a') + \sin h \sin h' \tag{65}$$

From [105], the spectral irradiances, $I_o(\lambda)$, at *0.53 μm,* and *1.06 μm* are listed in Tab.5.

This formulation notwithstanding, *solar direct radiation at ground level*, where the LIDAR receiver may be sited, results overestimated since eq.(64) does not account for scattering and atmospheric attenuation of the radiation. Consequently, the lower the Sun, the higher the attenuation because the radiation has to travel further. This effect can be estimated by using the concept of atmospheric mass, m_a, which is directly related to the zenithal angle, z (z=90-h). Ref.[105] lists extensive tables of irradiance figures, $I_{o(\lambda)}$, for different atmospheric masses. Tab.5 illustrates two examples, where the atmospheric masses have been computed considering two Sun's elevation angles, a 15th January at noon, and a 15th June also at noon. These figures have been compared to the Sun's irradiances at these wavelengths.

λ	$I_o(\lambda)$ $Wm^{-2}\mu m^{-1}$	I(λ) 15th Jan		I(λ) 15th Jun		Moon (m_a=2)
		extra	direct	extra	direct	
530 nm	1842	879	475	1697	1223	2.6e-3
1064 nm	653	319	267	616	546	2.3e-3

Tab.5 Radiance levels at the Nd:YAG operating wavelegths.

Yet, there is another kind of Sun's radiation, one has to account for. It is *the diffused component,* which is mainly caused by the scattering of Sun's radiation on the atmosphere. The concept of *global radiation* blends in a single term both the direct and the diffused component. The global and diffused components (denoted I_{glob} and I_{dif}, respectively) can be related on an horizontal plane via the turbidity factor, K_T

$$\frac{I_{dif}}{I_{glob}} = 1 - 1.13 K_T \tag{66}$$

It can be interpreted as the ratio of global radiation to the one that would be if the the atmosphere would not exist (this is precisely the extra-atmospheric component)

$$K_T = \frac{I_{glob}}{I_{ext}} \tag{67}$$

Likewise, the solar direct component can be obtained as follows

$$I = I_{glob} - I_{dif} \tag{68}$$

From eqs.(66) to (68), the global and diffused components can be assessed if it is used that

$$I_{glob}^2 = \frac{II_{ext}}{1.13} \tag{69}$$

$$I_{dif} = \left(\frac{II_{ext}}{1.13} \right)^{0.5} - I \tag{70}$$

It should be emphasized that the expressions given only apply over an horizontal plane. On inclined planes the following ones should be used:

$$I_{dif}(\beta) = \frac{1}{2}\left[1 + \cos\beta + \rho(1 - \cos\beta)\right] I_{dif}(0) \tag{71}$$

$$I_{glob}(\beta) = I(\beta) + I_{dif}(\beta) \tag{72}$$

Summing up, in the same way that laser beams are scattered by the atmospheric constituents such as clouds and fogs, so is Sun's radiance. Being the case, the models are based on statistical extrapolations that relate intrinsic parameters of the clouds and fogs (e.g. type and extension on the sky) with the air mass. The ratio of radiation with and without sky scattering effects is given as an extra loss [11].

5.4 Moon's radiation

A straightforward formulation to model Moon's radiation similar to the one used to model Sun's radiation has not been found in the literature. Yet, one can resort to tabulated figures versus the elevation angle of the Moon [109][45]. [105] provides Moon's irradiance for different atmospheric masses and wavelengths. Fig.34 from the same reference plots the spectral irradiance of the Moon for an atmospheric mass $m_a = 2$. Tab.5 lists *link-atmos* figures at the wavelengths of interest considering full moon and $m_a=2$. Were the LIDAR to be in operation at night, city lights (e.g from illuminated buildings and lamp-posts) may well outweigh Moon's radiance levels.

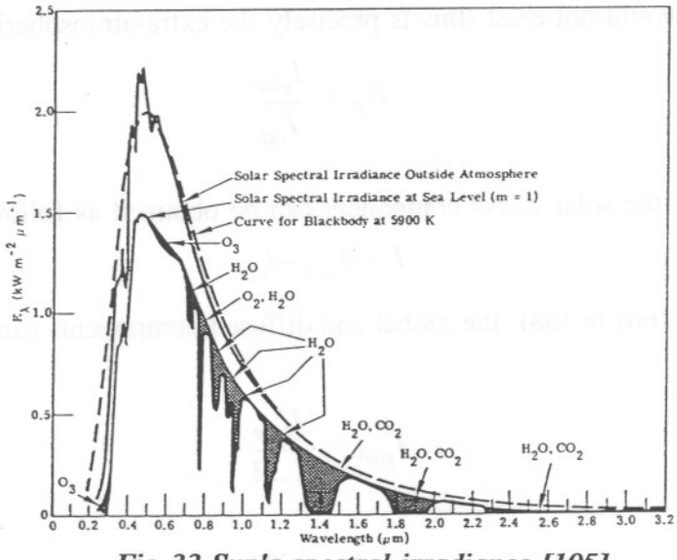

Fig.33 Sun's spectral irradiance [105].

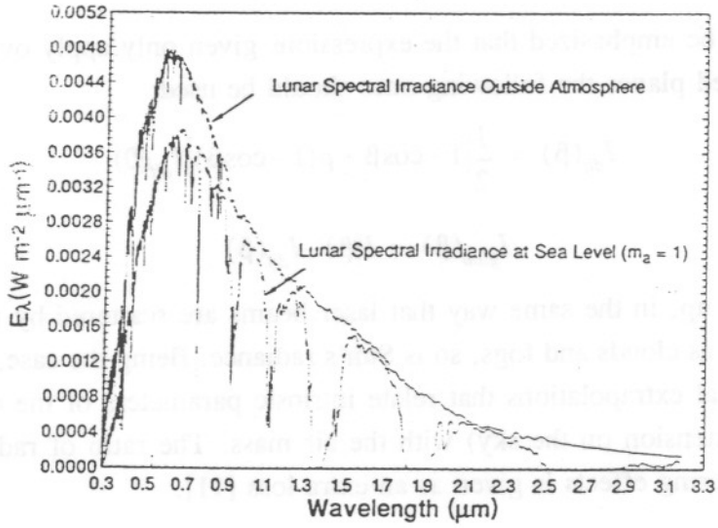

Fig.34 Spectral irradiance of the full moon at sea level for air mass m_a=2 [105].